tvst

Article

Advances in Imaging of Subbasal Corneal Nerves With Micro–Optical Coherence Tomography

Merle S. Schenk[1,2,*], Andreas Wartak[1,3,*], Verena Buehler[1,4], Jie Zhao[1], Guillermo J. Tearney[1,5,6], Reginald Birngruber[1,4,*], and Stefan Kassumeh[1,2,*]

[1] Wellman Center for Photomedicine, Massachusetts General Hospital, Boston, MA, USA
[2] Department of Ophthalmology, Ludwig-Maximilians-University Munich, Munich, Germany
[3] Department of Dermatology, Harvard Medical School, Harvard University, Boston, MA, USA
[4] Institute of Biomedical Optics, University of Luebeck, Luebeck, Germany
[5] Department of Pathology, Massachusetts General Hospital, Harvard Medical School, Boston, MA, USA
[6] Harvard-MIT Division of Health Sciences and Technology, Cambridge, MA, USA

Correspondence: Merle S. Schenk, Wellman Center for Photomedicine, 40 Blossom St, Boston, MA 02114, USA.
e-mail: merlesophies@gmail.com

Received: May 5, 2021
Accepted: October 10, 2021
Published: November 15, 2021

Keywords: corneal nerves; micro–optical coherence tomography; subbasal plexus

Citation: Schenk MS, Wartak A, Buehler V, Zhao J, Tearney GJ, Birngruber R, Kassumeh S. Advances in imaging of subbasal corneal nerves with micro–optical coherence tomography. Transl Vis Sci Technol. 2021;10(13):22, https://doi.org/10.1167/tvst.10.13.22

Purpose: To investigate the most peripheral corneal nerve plexus using high-resolution micro–optical coherence tomography (µOCT) imaging and to assess µOCT's clinical potential as a screening tool for corneal and systemic diseases.

Methods: An experimental high-resolution (1.5 × 1.5 × 1 µm) µOCT setup was applied for three-dimensional imaging of the subbasal nerve plexus in nonhuman primates (NHPs) and swine within 3 hours postmortem. Morphologic features of subbasal nerves in µOCT were compared to β3 tubulin-stained fluorescence confocal microscopy (FCM). Parameters such as nerve density, nerve distribution, and imaging repeatability were evaluated, using semiautomatic image analysis in form of a custom corneal surface segmentation algorithm and NeuronJ.

Results: Swine and NHP corneas showed the species-specific nerve morphology in both imaging modalities. Most fibers showed a linear course, forming a highly parallel pattern, converging in a vortex with overall nerve densities varying between 9.51 and 24.24 mm/mm^2. The repeatability of nerve density quantification of the µOCT scans as approximately 88% in multiple image recordings of the same cornea.

Conclusions: Compared to the current gold standard of FCM, µOCT's larger field of view of currently 1 × 1 mm increases the conclusiveness of density measurements, which, coupled with µOCT's feature of not requiring direct contact, shows promise for future clinical application. The nerve density quantification may be relevant for screening for systemic disease (e.g., peripheral neuropathy).

Translational Relevance: Technological advances in OCT technology may enable a quick assessment of corneal nerve density, which could be valuable evaluating ophthalmic and systemic peripheral innervation.

Introduction

Originating from the ophthalmic branch of the trigeminal nerve, corneal nerve fibers enter the stroma from the corneoscleral limbus and the ciliary body and divide into smaller branches to form the stromal plexus.[1] Following innervation of the middle and anterior stroma, the fibers penetrate the Bowman membrane (BM) at a 90° angle and form a dense network in the basal epithelium, called the subbasal nerve plexus (SBP), before they terminate in fine ends of about 0.5 µm thickness.[2] This vast nerval network comprises approximately 700 free nerve endings per square millimeter, making the cornea one of the most densely innervated tissues of the human body.[3]

The corneal nerves are of particular relevance for various corneal functions, namely, the eyelid reflex via their sensory properties, wound healing, and the lubrication of the ocular surface with tear fluid.[4] A decline

in the number of corneal nerves, particularly of the most peripheral epithelial nerves, can contribute to dry eye syndrome or neurotrophic keratopathy.[5,6]

Damage to the corneal nerves is not only relevant in ophthalmology but can also provide important diagnostic information about systemic diseases. For example, in diabetes mellitus (DM), a decline in peripheral nerve density is observed long before symptomatic onset of the illness.[3] A decrease in nerve density of peripheral nerves is known to co-occur with corneal denervation.[7] Consequently, direct clinical availability of optical imaging modalities able to visualize epithelial nerves in the transparent cornea could potentially be applied for assessment of surrogate parameters (e.g., nerve density, nerve distribution), reflecting the peripheral nerval state in the whole body. A common pathology that can cause such damage is diabetic neuropathy, with a prevalence of 30% to 50% in patients with DM.[8,9] Based on existing in vivo confocal microscopy (IVCM) studies, it can be assumed that peripheral nerves in the cornea hold an important prognostic ability for diabetic neuropathy and can be used to optimize treatments.[10,11] Accurate detection, characterization, and quantification of nerve morphology are important to identify high-risk patients, monitor progress, and initiate therapeutic adaptations.[12] The clinical significance of corneal nerve assessment was confirmed in a clinical study, which demonstrated the morphologic restoration of corneal nerve architecture when blood sugar levels are stabilized or lowered.[13] Corneal nerve axon degeneration with a retrograde course has also been described for several neurologic diseases such as ischemic stroke[14] and Parkinson disease.[15] Another important disease is medication-induced polyneuropathy, as a variety of pharmacologic agents, such as chemotherapeutics or antibiotics, decrease peripheral nerve density as an unwanted side effect.[16]

IVCM is the current gold standard in the field of corneal nerve imaging, enabling imaging of small diameter-nerves at cellular levels.[17] However, one factor hindering IVCM from becoming a clinical standard is its small field of view (FoV) of only 400 × 400 µm.[10] Typically, several images need to be recorded side-by-side to investigate a meaningful area of the cornea. The resultant long imaging time requires high compliance from patients.[18] Another limiting factor is IVCM's requirement of direct corneal surface contact, which is only possible under local anaesthesia.[19] A noninvasive and fast imaging technology that can efficiently map the nerval microstructure without contacting the cornea has the potential to significantly increase the adoption of corneal nerve imaging measurement.

Optical coherence tomography (OCT) has already found broad clinical application in anterior and posterior ophthalmic imaging.[20] However, to date, commercially available spectral-domain (SD) OCT lacks the resolution to allow for investigation of the fine corneal subbasal nerve fibers (SNFs). Recent OCT technology advances increasing both axial and transverse resolution toward the low single micrometer regime have demonstrated visualization of the SBP ex vivo and in vivo.[21–29] Although volumetric imaging of the SBP has been available with IVCM for quite some time,[30] advantages of recently developed micro-OCT (µOCT) compared with IVCM include higher imaging speeds that enable increased volumetric data acquisition, its comparably larger FoV, and its noncontact operation. In addition, all OCT models acquire volumetric data, in contrast to fluorescence confocal microscopy (FCM), which is a single-plane imaging modality.

In this study, we present the quantification of the SBP in different ex vivo mammalian samples, namely, swine and nonhuman primate (NHP), using high-resolution µOCT. Furthermore, we discuss the differences in anatomy and morphology of subbasal nerves across the two species and present a semiautomatic quantification process, which is then compared to SNF structures visualized with FCM of nerve-specific $\beta 3$ tubulin staining. Possible clinical uses and necessities to be implemented into the µOCT setup are outlined.

Methods

Animal Tissue

For corneal imaging and staining of the SBP, excised swine (Yorkshire/Landrace hybrid; Yucatan minipig; $n = 16$) and NHP (cynomolgus macaques; $n = 10$) corneas were used. The eyes were obtained from in-house facilities in accordance with the regulations of the Institutional Animal Care and Use Committee (Approval ID: 2019N000082 and 2018N000214), Massachusetts General Hospital (Boston, MA, USA). The eyes were enucleated and imaged within 1 to 3 hours after euthanasia. To keep the specimen moist until imaging, the eyes were kept in phosphate-buffered saline (PBS; Thermo Fisher Scientific, Waltham, MA, USA). The samples were then placed in a custom-designed wholemount eye holder or a corneoscleral disc was excised using scalpel and keratoplasty scissors (Katena Products, Inc., Parsippany, NJ, USA) and placed in an anterior eye chamber. Throughout the study, the area of interest for µOCT imaging was the apex of the cornea, as the most central part. Both models were attached to a water column to

maintain a physiologic intraocular pressure of approximately 18 mm Hg. During imaging, the samples were frequently covered with a 20% w/v dextran (molecular weight, 450,000–600,000; Sigma-Aldrich, St. Louis, MO, USA) in PBS solution to prevent desiccation.

Imaging

µOCT Imaging

µOCT imaging was conducted on a benchtop spectral domain prototype. A detailed description of the experimental setup can be found elsewhere.[31] In short, the prototype operates at a central wavelength of 800 ± 150 nm at line scan rate of 70 kHz. Experiments were conducted at a working distance of the µOCT objective lenses of 20 mm and a total laser power varying between 10 mW and a maximum of 20 mW. The imaging consistently focused on the apex as the corneal center with a FoV ranging from 500 × 500 µm to 1000 × 1000 µm, resulting in volumetric scan times between 3.5 and 14.3 seconds. A transverse resolution of ∼1.5 µm and an axial resolution of just below 1 µm in corneal tissue were achieved with a NIR infinity-corrected 0.4 NA plan-apochromat objective (Mitutoyo, Kanagawa, Japan).

Confocal Microscopy Imaging

Stained corneas were imaged with a commercially available automated laser scanning fluorescence confocal microscope (Fluoview FV1000 coupled IX81; Olympus, Tokyo, Japan). Magnifications used were 10×, 20×, and 60× (NA 0.40, 0.75, and 1.2, respectively). Recordings were conducted with a function called "Multi Area Time Lapse" (Fluoview FV1200; Olympus), imaging each tile individually in sequence, eventually creating a large mosaic image of either the whole cornea or differently sized excerpts around the corneal center, as this was the area of interest imaged with the µOCT.

Sample Preparation and Immunohistochemistry

Immunostaining of the corneal nerves for β3 tubulin was performed as described previously with some modifications.[32,33] Immediately after the µOCT imaging, the excised corneas were fixed in 4% paraformaldehyde (Sigma-Aldrich) for 1.5 hours. After rehydration in PBS overnight at 4°C, the corneas were placed in PBS supplemented with 1% Triton X-100 (Electron Microscopy 190 Science, Hatfield, PA, USA) three times for 20 minutes. This was followed by a blocking period of two times 1 hour and two times 5 minutes with a PBS-based blocking buffer containing 10% fetal bovine serum (Life Technologies, Carlsbad, CA, USA), 3% bovine serum albumin (Sigma-Aldrich), and 1% Triton X-100 to increase antibody specification to nerval proteins. These steps were all carried out with rocking at room temperature. Flattening of the cornea was achieved by straight scalpel cuts from the corneal periphery toward the center. Incubation with a purified antitubulin β3 primary antibody (#801202; USA Biolegend, San Diego, CA, USA), 1:1000 diluted in blocking solution, was carried out for 4 days on a gentle rotation device at 4°C to mark the nerval skeleton. After the incubation period, the corneas were again blocked with the aforementioned blocking solution three times for 1 hour, followed by three washing steps in PBS with 1% Triton X-100 for 10 minutes each. As a next step, samples were incubated with goat anti-mouse antibody connected to Alexa Fluor 647 (cat. 21235, Thermo Fisher Life Technologies, Carlsbad, CA, USA) 1:200 diluted in blocking solution for 2 days with gentle rotation at 4°C and light-protected in the dark to avoid fluorescence bleaching. Subsequently, the corneas were washed three times for 30 minutes in PBS 1% Triton X-100 and three times for 15 minutes in pure PBS. The samples were mounted between an objective slide and a cover glass with ProLong Glass antifade reagent without DAPI (cat. P36930; Thermo Fisher Scientific). Due to the thickness of the sample, the cover glass was taped to the objective slide on both sides and sealed with transparent nail polish to prevent the sample from drying out. Before imaging with the FCM, the slides were kept at 4°C in the dark for a few hours to equilibrate.

Image Postprocessing and Data Analysis

Due to the physiologic curvature of the cornea and pathlength differences introduced by the objective lens for off-axis scanning angles, the curved volumetric µOCT scan data were segmented at the corneal surface and flattened by an automatic algorithm, as described elsewhere,[31] in order to allow for visualization of the single-nucleotide polymorphism (SNP) in a single two-dimensional (2D) image. The reformatted 2D image comprised nearly all visible SNFs and was used for the 2D tracking. Image analysis of µOCT and FCM was then carried using the ImageJ[34] (ImageJ 1.50c4, Wayne Rasband; National Institutes of Health, Bethesda, MD, USA) software plugin NeuronJ[35] for semiautomatic neuron tracking in 2D images. This requires manual identification of a neuron in a binary map. Once identified, the program automatically continues the course of the neuron through the image, thus

calculating the nerve length (in µm). The density was then calculated using the sum nerve length of all traces in relation to the image size and converted to mm/mm^2. Several representative µOCT volumes were additionally tracked with a more-dimensional tracking tool, namely, the ImageJ plugin Simple Neurite Tracer (SNT).[36] This tool also requires manual identification of a neurite, but instead of following the neurite course within just one slice, it additionally identifies adjacent nerves within a three-dimensional (3D) neighborhood, which in turn increases the required analysis time. Despite the ability to search more dimensions for nerval structures, the traces are also given as a length instead of a 3D volume. Therefore, a comparison between the two analysis tools was made to investigate whether SNT is capable of identifying additional nerval structures within the µOCT stack or whether the NeuronJ results are equally reliable but much faster to attain.

Results

SBP Morphology in Swine and NHP Corneas

Swine

Figure 1 displays representative µOCT en face images of swine corneas in comparison to FCM stained with β3 tubulin. The images in Figures 1A–C, E–G show the µOCT en face projections (maximum intensity projection over a depth of ~3 µm). In semiautomatic traces with NeuronJ (Figs. 1A–D), both µOCT and FCM show a homogeneous nerve distribution pattern with high fiber density. Due to the limited FoV, 1:1 matching of location for both modalities was impossible, but the respective images originate from the same area of the cornea. The SNFs run mostly parallel in a 7–2, 10–1, and 5–3 o'clock direction. The nerves are in close vicinity to each other and occasionally form anastomoses. Figures 1E–H show an irregular, winding, or tortuous nerve pattern. Although most nerves in the µOCT image run somewhat parallel in a vertical direction, several perpendicular courses, seemingly connecting linear SNFs, can be observed. Figure 1H portrays a FCM image with a similar irregular tortuous pattern. However, the FCM image also presents additional, finer irregular structures that cannot be observed in the µOCT (Figs. 1E–F). Overall, the FCM images in Figure 1D portray nerves with varying thicknesses, whereas the nerve structures in the µOCT image all show similar thicknesses.

NHPs

Figure 2 shows the nerval morphology of an exemplary NHP cornea, with the µOCT en face image in Figure 2A and the nerve traces and binary skeleton map in Figures 2B and 2C, respectively. In

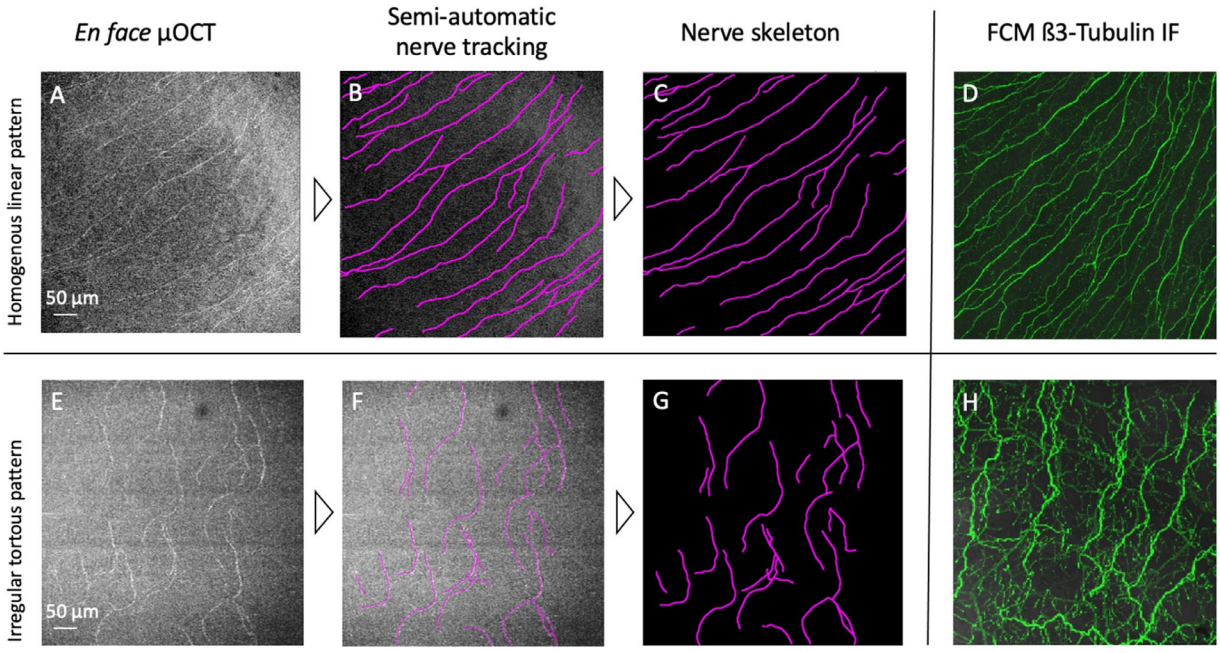

Figure 1. Swine en face µOCT images of different characteristic morphology features compared to FCM. (A, E) Segmented en face µOCT raw image. (B, F) Semiautomatic nerve tracking with NeuronJ. (C, G) Nerve skeleton of nerve traces (in *magenta*). (D, H) β3 Tubulin-stained FCM images. *Scale bars*: 50 µm.

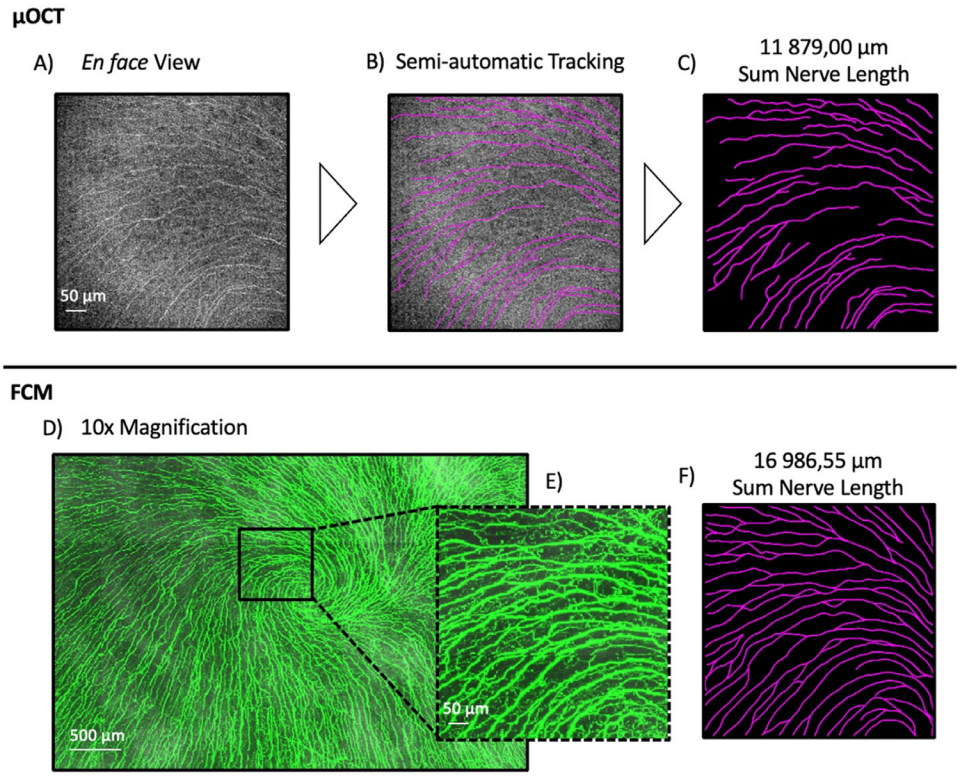

Figure 2. Comparison of µOCT and FCM nerve quantity, both showing the same morphologic features in NHPs. (A) Segmented en face µOCT image. (B) Semiautomatic nerve tracking, tracked with NeuronJ. (C) Nerve skeleton and sum nerve length. (D) FCM 10× magnification/NA 0.40. (E) FCM excerpt of vortex proximate nerves. (F) Nerve skeleton and sum nerve length.

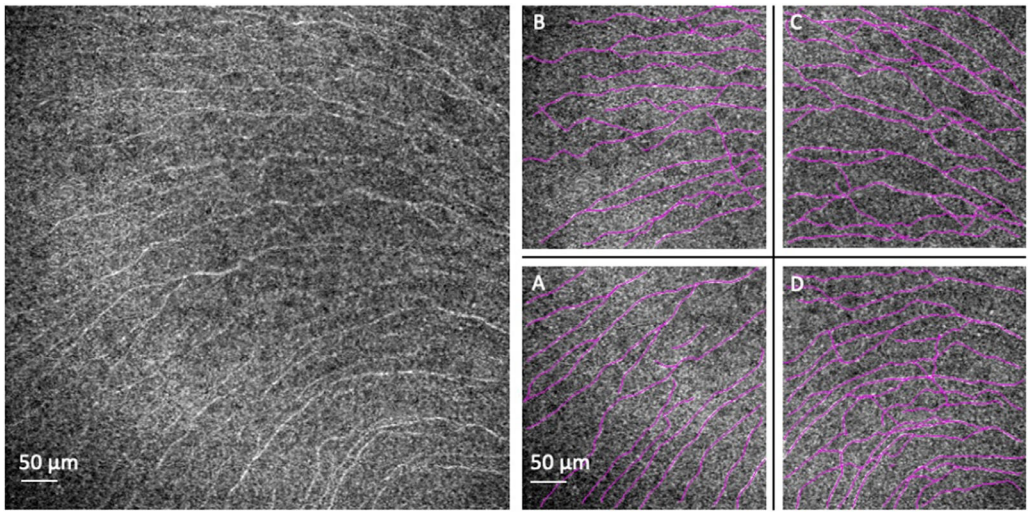

Figure 3. Investigating homogeneity of SNF distribution within µOCT FoV, en face µOCT, semiautomatic nerve segmentation, and quantitative evaluation with NeuronJ. (A) 2,514.07 µm. (B) 2,991.03 µm. (C) 3,741.10 µm. (D) 3,971.74 µm. *Scale bars*: 50 µm.

general, NHP corneas showed a dense and regular subbasal nerve pattern. In Figure 2, the nerves emerge from the periphery and converge in a vortex, found to be commonly located in the center of the cornea. Figure 2 shows a vortex proximate area with increasing curvature toward 4–5 o'clock. Figure 2D displays a larger area of an NHP cornea, at a 10× magnification, allowing the µOCT FoV to be matched with its location in the plexus. The pertinent structure of the vortex was used for orientation

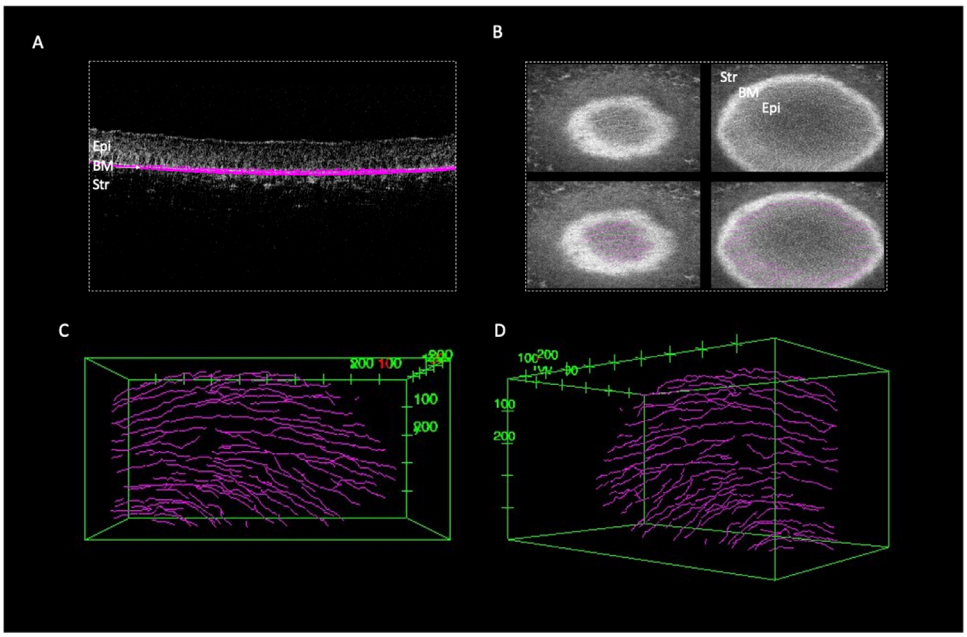

Figure 4. SNF tracking in NHP with Simple Neurite Tracer, marked in *magenta*. (A) 3D model view of SBP fiber distribution and corneal layers in a single plane embedded in the lower epithelium. (B) En face view of two different µOCT slices without and with marked SNFs in *magenta*. (C, D) 3D model view µOCT from different angles. Epi, epithelium; Str, stroma.

to identify comparable images in FCM, as shown in Figure 2E. Figure 2F shows the binary nerve skeleton map of the semiautomatic traces of the FCM region of interest in Figure 2E with the total nerve length. Images in Figures 2C and 2F were measured to have a sum length of nerves of 11,879.00 µm and 16,986.55 µm in the µOCT and FCM image, respectively.

Existing studies have assumed that the SNF density increases toward the center close to the vortex, which was also observed in the en face µOCT image in Figure 2.[4] Therefore, Figure 3 shows the previously described en face µOCT image, additionally split into four equally sized quadrants and tracked semiautomatically. The sum nerve length of the quadrants was quantified individually and compared in order to evaluate the distribution of nerve fibers within one cornea region within the FoV. The values varied between 2514 µm in quadrant A and 3971 µm in quadrant D. The latter is also the closest to the vortex. Therefore, the nerve density differed within the FoV of 706.6 × 706.6 µm, varying up to 36.7% between quadrants 1 and 4.

Sum Nerve Length and Nerve Density

Table 1 shows quantitative evaluation results of sum nerve length and nerve density in the SBP from five different corneas for the two different species investigated, namely, swine and NHP. As previously described, segmented µOCT images were used and the sum nerve length was quantified with NeuronJ.

Table 1. Nerve Density of the SBP in Swine and NHP Corneas

	Swine		NHP	
Cornea	Sum Nerve Length, µm	Nerve Density, mm/mm^2	Sum Nerve Length, µm	Nerve Density, mm/mm^2
1	6810	13.90	7530	15.37
2	8360	17.06	9720	19.84
3	6590	13.45	10,090	20.59
4	7530	15.37	8310	16.96
5	4660	9.51	11,880	24.24
Mean	6790	13.86	9510	19.41

Table 2. Comparison of 2D and 3D Tracking Tool for Nerve Density Quantification

	Analysis Tool and Dimension	
Sample	3D SNT, mm/mm^2	2D NeuronJ, mm/mm^2
1	26.73	26.36
2	26.07	22.64
3	15.94	14.56

Nerve density quantification of the SBP (in mm/mm^2), quantified in the 3D tracking program SNT in comparison to the 2D program NeuronJ in three swine and NHP corneas (samples 1 and 2 = NHP, sample 3 = swine) with µOCT recordings (700 × 700 µm image size).

The mean (±1 standard deviation) was measured to be 13.86 mm/mm^2 (±2.51 1/mm) and 19.41 mm/mm^2 (±3.08 1/mm) in swine and NHPs, respectively. The NHP SBP density overall was significantly higher (Mann–Whitney *U*-test; $P = 0.0397$) compared to swine.

2D Versus 3D Tracking of SBP

To investigate whether tracking in 2D en face µOCT images achieves comparable results to volumetric tracking in 3D, we performed an analysis and compared the 2D nerve tracking software NeuronJ with the 3D tracking software SNT on identical data sets. Initially, we investigated the SBP fiber distribution in 3D using SNT, shown in Figure 3. Figure 3A shows an overlay of the 3D tracking results over a cross-sectional view of the volumetric µOCT rendering, displaying a planar plexus above the BM. Figure 3B shows two different µOCT slices of the en face stack of the unflattened data set. The upper row includes the raw µOCT image, whereas the lower row shows marked SNFs in magenta together with the corneal tissue surroundings. Figures 3A and 3B also show the stroma, BM, and epithelium. Figures 3C and 3D depict 3D tracking results in a frontal and a 45-degree view of the SBP nerve skeleton, without the surrounding corneal tissue. Therefore, multiple µOCT data sets were tracked in both representations (2D, 3D; $n = 3$) in order to make quantitative claims; no statistically significant difference (Mann–Whitney *U*-test, $P = 0.70$) in sum nerve length (mm) per square millimeter was found.

Repeatability of µOCT Imaging and SNF Quantification

Table 3 shows the variation in sum nerve length analysis when a cornea is imaged repeatedly with the µOCT setup, with a new alignment and an approximate time difference of 10 to 15 minutes between recordings. Three swine and two NHP corneas were imaged multiple times close to the corneal apex, and the sum length of SNF was determined in micrometers within a consistent FoV of 700 × 700 µm. Standard deviations were calculated relative to the mean sum length. The relative standard deviation percentage varied between 7.05% and 16.90% with an average relative standard deviation of 11.24%. All samples except for one NHP sample (sample 2) showed a continuous decrease in the quantified nerve density between the first scan and the fourth.

Discussion

In this article, we present the capability to quantify the subbasal nerve plexus and present the species-specific nerve morphology of swine and NHP corneas ex vivo with a µOCT in a repeatable manner. Thus, our results corroborate the µOCT's potential as a diagnostic tool, which might enable future in vivo screening of corneal and systemic diseases after further research and therefore might detect peripheral nerve thinning in patients in early stages.

The growing interest in corneal nerves has fueled technological advances in full-field (FF) and SD-OCT resolution.[21–29,31] In this study, we were able to visualize the SBP and recurring morphologic features, namely, vortex, linear, and irregular tortuous nerve patterns in both species, swine and NHP, with the µOCT. These anatomic characteristics were described before using immunostaining,[37] IVCM,[38] and OCT.[21–29,31] Interestingly, the vortex was easier to discern in NHP corneas, while swine corneas showed a more centrifugal distribution pattern. This finding is in line with a recent study by Marfurt et al[4] that showed that the subbasal nerve vortex was present in 100% of NHP corneas stained with antiserum against neurotubulin and could not be observed in domestic pig corneas. Thus, in terms of morphologic findings, µOCT as a noncontact and fast imaging modality seems to keep up to its current gold-standard previous findings in IVCM.

Subbasal corneal nerve density, morphology, and tortuosity are of high interest in the clinical assessment of systemic diseases, particularly in diabetic neuropathy. A reduction of fiber density and branching as well as reduced corneal nerve tortuosity correlates with the severity of systemic/somatic neuropathy in diabetic patients.[39] Previous studies further revealed decreased fiber length not only in diabetic patients with peripheral polyneuropathy but also in diabetic patients

Table 3. Repeatability Evaluation of SBP Density

	Swine, mm/mm^2			NHP, mm/mm^2	
Characteristic	Sample 1			Sample 2	
Scan 1	19.90	15.36	Sample 3	Sample 1	Sample 2
Scan 2	17.07	15.94	13.45	26.07	14.41
Scan 3	16.61	14.77	12.26	26.72	17.34
Scan 4	14.78	13.49	10.42	23.89	13.90
Standard deviation, 1/mm	2.12	1.05	—	23.43	19.84
Mean, mm/mm^2	17.09	14.89	1.53	1.61	2.77
RSD	0.12	0.07	12.04	25.03	16,387.45
%RSD	12.39	7.05	0.13	0.07	0.17
Average %RSD	11.24		12.67	7.21	16.90

Repeatability evaluation of SBP density quantification (in mm/mm^2) of three or four repeated µOCT scans of swine ($n = 3$) and NHP ($n = 2$) corneas. RSD, relative standard deviation.

without polyneuropathy (PNP) and even in prediabetic patients.[40,41] These findings further underline the clinical relevance of a diagnostic tool to possibly prescreen predestined patients before somatic disease onset of diabetes mellitus. First pioneering studies on human corneas suggest the FF-OCT to be capable of imaging subbasal corneal nerves in vivo.[21,24,25,29] We present a semiautomatic and repeatable method to analyze corneal nerve fiber length, density, and morphology in a considerable FoV in two mammalian species ex vivo. In vivo, the gathered information may be sufficient to allow experienced clinicians to depict pathologic changes in SBP density immediately.

Additional automation in the postprocessing and analysis process is needed to facilitate the integration of µOCT into a cost-effective clinical setting (e.g., using deep learning algorithms currently tested for segmentation of subbasal nerves in IVCM images).[42] The imaging speed, which is restricted by camera technology and further potentially limited through signal-to-noise ratio (SNR) constraints, imposes a limitation on µOCT imaging. In contrast to FF-OCT, µOCT has also only been demonstrated for considerably small FoVs to date. Furthermore, clinical translation of corneal µOCT to humans in vivo will require adjustment to mitigate subject motion and to decrease illumination power.

Even with a FoV of ~700 × 700 µm, which is nearly four times the FoV of IVCM (at 400 × 400 µm), we found a varying corneal nerve fiber distribution in adjacent sections of one single cornea. Similarly, Winter et al[43] reported significant differences of corneal nerve fiber length of the SBP within single frames of one cornea of healthy human participants when using the Rostock Cornea Module. The Maastricht study found a reduction of corneal nerve fiber length of 14% in diabetic patients when compared to patients with a normal glucose metabolism using matched IVCM images with a FoV of up to 1.6 × 1.6 mm but with a high standard deviation.[41] Therefore, it should be noted that current evaluation of single en face frame µOCT may lead to a significant examiner bias when trying to derive information for clinical diagnosis. Whether the mean corneal nerve fiber length derived from a composite image of several µOCT scans allows for clinical disease assessment (e.g., in early stages of diabetic neuropathy) has yet to be discerned.

Besides the potential of SBP density evaluation through µOCT imaging in diabetic care, it may be used as a staging and treatment monitoring tool in dry eye syndrome (DES). Liu et al[44] found a significant correlation between corneal nerve width and the Ocular Surface Disease Index by IVCM. In addition, DES is a recurring complication after refractive surgery, like laser in situ keratomileusis and small-incision lenticule extraction, mainly caused by a decrease of nerve density due to the typical femtosecond laser-assisted cutting patterns.[45] Using µOCT, corneal subbasal nerve density may be used to prescreen patients prior to refractive surgery. Thus, patients with a higher tendency of postoperative DES may be targeted earlier, or in severe cases, another surgical approach may be discussed.

Current limitations of the study include the relatively small sample size and the inability to match the exact imaged location between the two different modalities and the two species. Thus, reliable comparisons between FCM and µOCT or nerval densities for different species cannot be drawn. Furthermore, it is unknown to what extent the postmortem denervation processes, which do not occur in a uniform manner,[46] and the lack of physiologic corneal hydration might

have influenced the quantitative results due to the several hours' duration between corneal excision and µOCT imaging. Furthermore, the time lapse between µOCT recordings of the same sample, together with the varying degree of desiccation, might have led to a relatively high standard deviation of averagely 11.24%. These aforementioned external factors will play a minor role when advancing our studies to in vivo imaging. Future investigations further aspire to standardize nerve densities in health and under various corneal and systemic pathologic conditions.

To conclude, our study offers new insights on how to track SNFs and quantify the corneal nerve fiber length and density of the SBP repeatedly in NHP and swine corneas ex vivo. Furthermore, it corroborates µOCT's potential to become a clinical prescreening tool for systemic disease, causing peripheral nerve degeneration, such as diabetes mellitus.

Acknowledgments

The authors thank Jermaine Henderson (Wellman Center for Photomedicine, MGH) and Brandon Apoo (Wellman Center for Photomedicine, MGH) for technical assistance and Christiane Fuchs (Wellman Center for Photomedicine, MGH) for assistance with immunostaining.

Disclosure: **M.S. Schenk**, None; **A. Wartak**, None; **V. Buehler**, None; **J. Zhao**, None; **G.J. Tearney**, SpectraWave (I), SpectraWave (C), Vertex (F), CNUSA Biotech Holdings (F), Astra Zeneca (F), Translate Bio (F), WayVector (F), Xsphera Biotech (F); **R. Birngruber**, None; **S. Kassumeh**, None

* MSS and AW are co-first authors. RB and SK are co-senior authors.

References

1. He J, Bazan NG, Bazan HE. Mapping the entire human corneal nerve architecture. *Exp Eye Res*. 2010;91(4):513–523.
2. Muller LJ, Marfurt CF, Kruse F, Tervo TM, et al. Architecture of human corneal nerves. *Invest Ophthalmol Vis Sci*. 1997;38(5):985–994.
3. Cruzat A, Qazi Y, Hamrah P. In vivo confocal microscopy of corneal nerves in health and disease. *Ocul Surf*. 2017;15(1):15–47.
4. Marfurt C, Anokwute MC, Fetcko K, et al. Comparative anatomy of the mammalian corneal subbasal nerve plexus. *Invest Ophthalmol Vis Sci*. 2019;60(15):4972–4984.
5. Cruzat A, Witkin D, Baniasadi N, et al. Inflammation and the nervous system: the connection in the cornea in patients with infectious keratitis. *Invest Ophthalmol Vis Sci*. 2011;52(8):5136–5143.
6. Giannaccare G, Pellegrini M, Bernabei F, et al. In vivo confocal microscopy automated morphometric analysis of corneal subbasal nerve plexus in patients with dry eye treated with different sources of homologous serum eye drops. *Cornea*. 2019;38(11):1412–1417.
7. Bikbova G, Oshitari T, Baba T, Yamamoto S. Neuronal changes in the diabetic cornea: perspectives for neuroprotection. *Biomed Res Int*. 2016;2016:5140823.
8. Callaghan BC, Cheng HT, Stables CL, Smith AL, Feldman EL. Diabetic neuropathy: clinical manifestations and current treatments. *Lancet Neurol*. 2012;11(6):521–534.
9. Albers JW, Pop-Busui R. Diabetic neuropathy: mechanisms, emerging treatments, and subtypes. *Curr Neurol Neurosci Rep*. 2014;14(8):473.
10. Hamrah P, Qazi Y, Shahatit B, et al. Corneal nerve and epithelial cell alterations in corneal allodynia: an in vivo confocal microscopy case series. *Ocul Surf*. 2017;15(1):139–151.
11. Pritchard N, Edwards K, Russell AW, Perkins BA, Malik RA, Efron N. Corneal confocal microscopy predicts 4-year incident peripheral neuropathy in type 1 diabetes. *Diabetes Care*. 2015;38(4):671–675.
12. Pritchard N, Edwards K, Shahidi AM, et al. Corneal markers of diabetic neuropathy. *Ocul Surf*. 2011;9(1):17–28.
13. Jia X, Wang X, Wang X, et al. In vivo corneal confocal microscopy detects improvement of corneal nerve parameters following glycemic control in patients with type 2 diabetes. *J Diabetes Res*. 2018;2018:8516276.
14. Khan A, Akhtar N, Kamran S, et al. Corneal confocal microscopy detects corneal nerve damage in patients admitted with acute ischemic stroke. *Stroke*. 2017;48(11):3012–3018.
15. Kass-Iliyya L, Javed S, Gosal D, et al. Small fiber neuropathy in Parkinson's disease: a clinical, pathological and corneal confocal microscopy study. *Parkinsonism Relat Disord*. 2015;21(12):1454–1460.
16. Argov Z, Mastaglia FL. Drug-induced peripheral neuropathies. *Br Med J*. 1979;1(6164):663–666.
17. Grupcheva CN, Wong T, Riley AF, McGhee CN. Assessing the sub-basal nerve plexus of the living healthy human cornea by in vivo confocal

microscopy. *Clin Exp Ophthalmol*. 2002;30(3):187–190.
18. Selig B, Vermeer KA, Rieger B, Hillenaar T, Luengo Hendriks CL. Fully automatic evaluation of the corneal endothelium from in vivo confocal microscopy. *BMC Med Imaging*. 2015;15:13.
19. Chen S, Liu X, Wang N, et al. Visualizing micro-anatomical structures of the posterior cornea with micro-optical coherence tomography. *Sci Rep*. 2017;7(1):10752.
20. Fujimoto J, Swanson E. The development, commercialization, and impact of optical coherence tomography. *Invest Ophthalmol Vis Sci*. 2016;57(9):OCT1–OCT13.
21. Mazlin V, et al. In vivo high resolution human corneal imaging using full-field optical coherence tomography. *Biomed Opt Express*. 2018;9(2):557–568.
22. Tan B, et al. 250 kHz, 1.5 microm resolution SD-OCT for in-vivo cellular imaging of the human cornea. *Biomed Opt Express*. 2018;9(12):6569–6583.
23. Yao X, et al. In vivo corneal endothelium imaging using ultrahigh resolution OCT. *Biomed Opt Express*. 2019;10(11):5675–5686.
24. Mazlin V, Xiao P, Scholler J, et al. Real-time non-contact cellular imaging and angiography of human cornea and limbus with common-path full-field/SD OCT. *Nat Commun*. 2020;11(1):1868.
25. Auksorius E, Borycki D, Stremplewski P, et al. In vivo imaging of the human cornea with high-speed and high-resolution Fourier-domain full-field optical coherence tomography. *Biomed Opt Express*. 2020;11(5):2849–2865.
26. Wang L, Xiong Q, Ge X, et al. Cellular resolution corneal imaging with extended imaging range. *Opt Express*. 2019;27(2):1298–1309.
27. Canavesi C, Cogliati A, Mietus A, Qi Y, Schallek J, Rolland JP, Hindman HB., In vivo imaging of corneal nerves and cellular structures in mice with Gabor-domain optical coherence microscopy. *Biomed Opt Express*. 2020;11(2):711–724.
28. Hosseinaee Z, Tan B, Kralj O, et al. Fully automated corneal nerve segmentation algorithm for corneal nerves analysis from in-vivo UHR-OCT images. *SPIE BiOS*. 2019;60:167.
29. Mazlin V, Irsch K, Paques M, Sahel JA, Fink M, Boccara CA. Curved-field optical coherence tomography: large-field imaging of human corneal cells and nerves. *Optica*. 2020;7(8):872.
30. Muller LJ, Irsch K, Paques M, Sahel JA, Fink M, Boccara CA. Corneal nerves: structure, contents and function. *Exp Eye Res*. 2003;76(5):521–542.
31. Wartak A, Schenk MS, Buhler V, Kassumeh SA, Birngruber R, Tearney GJ. Micro-optical coherence tomography for high-resolution morphologic imaging of cellular and nerval corneal microstructures. *Biomed Opt Express*. 2020;11(10):5920–5933.
32. Jung Y, Ng JH, Keating CP, et al. Comprehensive evaluation of peripheral nerve regeneration in the acute healing phase using tissue clearing and optical microscopy in a rodent model. *PLoS One*. 2014;9(4):e94054.
33. Elhardt C, Wertheimer CM, Wartak A, et al. Stromal nerve imaging and tracking using micro-optical coherence tomography. *Transl Vis Sci Technol*. 2020;9(5):6.
34. Schneider CA, Rasband WS, Eliceiri KW. NIH Image to ImageJ: 25 years of image analysis. *Nat Methods*. 2012;9(7):671–675.
35. Meijering E, Jacob M, Sarria JC, Steiner P, Hirling H, Unser M. Design and validation of a tool for neurite tracing and analysis in fluorescence microscopy images. *Cytometry A*. 2004;58(2):167–176.
36. Longair MH, Baker DA, Armstrong JD. Simple Neurite Tracer: open source software for reconstruction, visualization and analysis of neuronal processes. *Bioinformatics*. 2011;27(17):2453–2454.
37. He J, Bazan HE. Neuroanatomy and neurochemistry of mouse cornea. *Invest Ophthalmol Vis Sci*. 2016;57(2):664–674.
38. Al-Aqaba MA, Dhillon VK, Mohammed I, Said DG, Dua HS. Corneal nerves in health and disease. *Prog Retin Eye Res*. 2019;73:100762.
39. Hossain P, Sachdev A, Malik RA. Early detection of diabetic peripheral neuropathy with corneal confocal microscopy. *Lancet*. 2005;366(9494):1340–1343.
40. Pritchard N, Edwards K, Dehghani C, et al. Longitudinal assessment of neuropathy in type 1 diabetes using novel ophthalmic markers (LANDMark): study design and baseline characteristics. *Diabetes Res Clin Pract*. 2014;104(2):248–256.
41. De Clerck EEB, Schouten Jsag, Berendschot Ttjm, et al. Reduced corneal nerve fibre length in prediabetes and type 2 diabetes: The Maastricht Study. *Acta Ophthalmol*. 2020;98(5):485–491.
42. Wei S, Shi F, Wang Y, Chou Y, Li X. A deep learning model for automated sub-basal corneal nerve segmentation and evaluation using in vivo confocal microscopy. *Transl Vis Sci Technol*. 2020;9(2):32.
43. Winter K, Scheibe P, Kohler B, Allgeier S, Guthoff RF, Stachs O. Local variability of parameters for characterization of the corneal

subbasal nerve plexus. *Curr Eye Res*. 2016;41(2): 186–198.
44. Liu Y, Chou Y, Dong X, et al. Corneal subbasal nerve analysis using in vivo confocal microscopy in patients with dry eye: analysis and clinical correlations. *Cornea*. 2019;38(10):1253–1258.
45. Toda I. Dry eye after LASIK. *Invest Ophthalmol Vis Sci*. 2018;59(14):DES109–DES115.
46. Pieri M, Maldonado AL, Ros MM, Massoni F, Ricci S, Vacchiano G. Post-mortem morphological alterations of human peripheral nerve. *Aust J Forensic Sci*. 2019;51(3):340–347.